AIAA Journal
Vol. 48, No. 10, October 2010

Gust Response for Flexibly Suspended High-Aspect Ratio Wings

Deman Tang,[*] Adam Grasch,[†] and Earl H. Dowell[‡]
Duke University, Durham, North Carolina 27708-0300

DOI: 10.2514/1.J050309

A theoretical aeroelastic study for a flexibly suspended high-aspect ratio wing aeroelastic model excited by gust loads is presented along with a companion wind-tunnel test. A flexible support system at the wing root has been constructed to simulate a rigid body mode. Structural equations of motion based on a nonlinear beam theory are combined with the ONERA aerodynamic model. Also, a dynamic perturbation analysis about a nonlinear static equilibrium is used to determine the small perturbation flutter boundary and structural natural frequencies. The effects of the flexible support system (bi-beam system) on the wing structural dynamics, the static aeroelastic displacement at root, nonlinear flutter, and gust response to a harmonic or a frequency sweep excitation are discussed. Also the effect of gust distribution along the span on the response is described based upon computations. The fair to good quantitative agreement between theory and experiment demonstrates that the present analysis method has reasonable accuracy.

Nomenclature

C_l = section lift coefficient
C_d = section drag coefficient
C_m = section torsional moment coefficient
c, $\bar{c}$ = wing chord and dimensionless chord, c/L
$\mathrm{d}F_v$, $\mathrm{d}F_w$ = section aerodynamic forces in lag and flap directions
$\mathrm{d}M_x$ = section pitch moment about elastic axis
E = modulus of elasticity
e = section mass center from elastic axis
G = shear modulus
g = gravitational constant
I_1, I_2 = flap and lag area moments
I_{x0}, I_{y0}, I_{z0} = moments of inertia for tip slender body
I_{mi} = ith generalized modal inertia moment for pitch
J = torsional stiffness constant
k_r = equivalent spring stiffness of bi-beam support
L = wing span
l = bi-beam span
M = tip mass of the wing
M_r = tip mass of the bi-beam support
m = mass per unit length of the wing
m_{vi}, m_{wi} = ith generalized modal mass for lag and flap
m_{sk} = kth generalized modal mass for bi-beam support
N_s = total number of structural modes
N_a = number of aerodynamic elements
q = state vector
S_k = kth generalized coordinates for bi-beam bending
s = bi-beam bending deflection
t = time
U = freestream velocity
V_j, W_j = jth generalized coordinates for lag and flap bendings
v = lag bending deflection
w = flap bending deflection
x, $\bar{x}$ = position coordinate along wing span and dimensionless, $\bar{x} = x/L$
y, $\bar{y}$ = position coordinate along bi-beam span and dimensionless, $\bar{y} = x/bl$
y_{ac} = distance of aerodynamic center of airfoil section from elastic axis
α_G = gust angle of attack
η_k = kth bending natural mode for bi-beam
θ_0 = steady angle of attack at root
ρ = air density
ν_j = jth lag natural mode
Φ_j = generalized coordinates for torsion
ϕ = twist about deformed elastic axis
φ_j = jth torsional natural mode of wing
ψ_j = jth flap natural mode
ω_g = gust frequency
ω_{rk} = kth bending natural frequency of bi-beam support
ω_{vj} = jth lag natural frequency of wing
ω_{wj} = jth flap natural frequency of flexibly suspended wing
$\omega_{\phi j}$ = jth torsional natural frequency of wing
$\dot{()}$ = $\mathrm{d}()/\mathrm{d}t$
$()'$ = $\mathrm{d}()/\mathrm{d}x$

I. Introduction

UNINHABITED HALE (high-altitude long-endurance) aircraft are of great current interest. High altitudes and low air densities dictate the use of a large wing area and a light structural design to increase lift and endurance, thus leading to the design of flexible high-aspect ratio wings. These wings undergo large deflections and the geometric structural nonlinearity becomes a very important factor that affects the aeroelastic stability and response of the HALE aircraft. Recent studies ([1–10]) have shown that there are significant differences in the flutter boundary, limit cycle oscillation (LCO) and gust response between a linear structural analysis and a nonlinear structural analysis.

In [6–8] an experimental high-aspect ratio wing aeroelastic model cantilevered at the root and with a tip mass was constructed and a wind-tunnel test conducted to measure flutter and limit cycle oscillations. For the companion computational model, the theoretical structural equations of motion are based on nonlinear beam theory [11] and the ONERA aerodynamic stall model [12]. Large static preflutter deformations in the vertical or torsional direction are

---

Received 4 November 2009; revision received 12 May 2010; accepted for publication 15 June 2010. Copyright © 2010 by the American Institute of Aeronautics and Astronautics, Inc. All rights reserved. Copies of this paper may be made for personal or internal use, on condition that the copier pay the $10.00 per-copy fee to the Copyright Clearance Center, Inc., 222 Rosewood Drive, Danvers, MA 01923; include the code 0001-1452/10 and $10.00 in correspondence with the CCC.

[*] Research Scientist, Department of Mechanical Engineering and Materials Science, Box 90300, Hudson Hall; demant@duke.edu.

[†] Senior Undergraduate Student and Pratt Fellow, Department of Mechanical Engineering and Materials Science, Box 90300, Hudson Hall; adg15@duke.edu.

[‡] William Holland Hall Professor, Department of Mechanical Engineering and Materials Science, Box 90300, Hudson Hall, Dean Emeritus, Pratt School of Engineering; dowell@ee.duke.edu. Honorary Fellow AIAA (Corresponding Author).

created by the gravity loading on the wing and a tip slender body. Also a steady angle of attack creates a static aerodynamic load on the wing.

Following [6], we construct a new HALE wing model to simulate a HALE wing flexibly suspended at its root. The boundary constraints at the wing root satisfy the following conditions:

1) The torsional rotation, $\phi(0,t)$ and chordwise displacement, $v(0,t)$ are zero.

2) An additional bi-beam support with a tip mass M_r is attached to the wing root in the flap direction. The flap displacement at the root, $w(0,t)$ is not zero, but $\frac{\partial w(0,t)}{\partial x}$ is zero. The HALE wing model is thus suspended in the vertical in such a way that it has a very low fundamental frequency with a mode shape that closely resembles a rigid body mode in the flap direction. The suspension frequency is adjusted by the bi-beam stiffness.

For the new HALE wing model, theoretical and experimental studies for the gust response to both a harmonic and a frequency sweep excitation have been carried out. Before the gust response analysis, preliminary theoretical studies are made for this HALE wing model to determine: 1) the natural frequencies, 2) the static aeroelastic displacement at the root, and 3) the nonlinear flutter boundary as a function of the root spring stiffness. A dynamic perturbation equation about a nonlinear static equilibrium is derived which is used to determine the natural frequencies and the small perturbation flutter boundary. For the nonlinear dynamic equations, a direct time marching method is used to calculate the static equilibrium solutions. Also this time marching method is used to determine the gust response when the gust load is added.

Gust excitation and response studies are the focus of this paper. The theoretical gust responses are compared with the measured data from the wind-tunnel test. The results provide insight into gust response phenomena and the effect of a rigid body like mode. Also the effect of gust distribution along the span on the response has been described based upon computations.

II. Experimental Wing Model and Root Flexible Suspension System

The experimental model includes two parts: 1) a high-aspect ratio wing with slender body at the wing tip, and 2) a adjustable root flexible suspension. The wing is rectangular, untwisted and flexible in the flap, lag and torsional directions. The wing is constructed from a precision ground flat steel spar with mass uniformly distributed along the wing span. The spar is 45.72 cm in length, 1.27 cm in width, and 0.127 cm in thickness. It is inserted tightly (clamped) into a wing root mechanism. To reduce torsional stiffness, the spar has multiple thin flanges along the span. The flange width is 0.127 cm and it is 0.318 cm in deep. There are 2×33 flanges uniformly and symmetrically distributed along the wing span and center line of the spar. There are 18 pieces of NACA 0012 airfoil plate uniformly distributed along the span. The pieces of the airfoil plate are made of aluminum alloy with 0.254 cm thickness. A precision aerodynamic contour of the wing model is obtained. Each airfoil plate has a slot 1.27 cm in width and 0.127 cm in thickness at the symmetry line. The spar is inserted through these airfoil plate slots and they are permanently bonded together. Each space between two airfoil plates is filled with a light wood (balsa) covering the entire chord and span which provides the aerodynamic contour of the wing. This wood provides a slight additional mass and a small addition to the bending and torsion stiffness.

A slender body is attached to the elastic axis of the wing tip. The slender body is an aluminum bar, 3/8 inch in diameter and 4 in. in length. A paraboloidal forebody and an aftbody with 0.45 in. length are fixed to two ends of the bar. The forebody and aftbody are made of brass.

The slender body is symmetrical and is designed to provide enough torsional inertia to reduce the natural torsional frequency sufficiently to induce flutter in the higher velocity range of the wind tunnel. All testing reported here is for flow velocities below the flutter speed, however.

The wing root is fixed on a socket (a rigid aluminum plate) at the end of the flexible suspension system. This is mounted outside of the wind tunnel at the top. The flexible suspension system consists of a bicantilever beam made of two aluminum leaf-spring which are 0.0508 cm thick, 4.445 cm wide and variable long from 10.5 to 30.5 cm. The socket allows movement in the flap direction and is clamped in the chordwise and torsion directions. The attached spring stiffness at the root, k_r, can be adjusted when the bicantilever beam span length changes. The connection between the wing root and the socket allows a change of the steady angle of attack, θ_0, at the root, i.e., $\theta_0 = 0, 1$, and 2°. Figures 1a and 1b show the photographs of the aeroelastic wing model with the flexibly suspended root support and the details of the wing model construction.

A rotational velocity displacement transducer, R30, is used to measure the displacement of wing root. The angular displacement transducer was calibrated and showed excellent linear response characteristic and high sensitivity.

Two micro-accelerometers are mounted near the elastic axis of the midspan and tip of the wing which are used to measure the gust flap responses. When the mounted tip accelerometer is rotated 90°, we can measure the gust lag response. Another micro-accelerometer is mounted near end of the slender body which is used to measure the

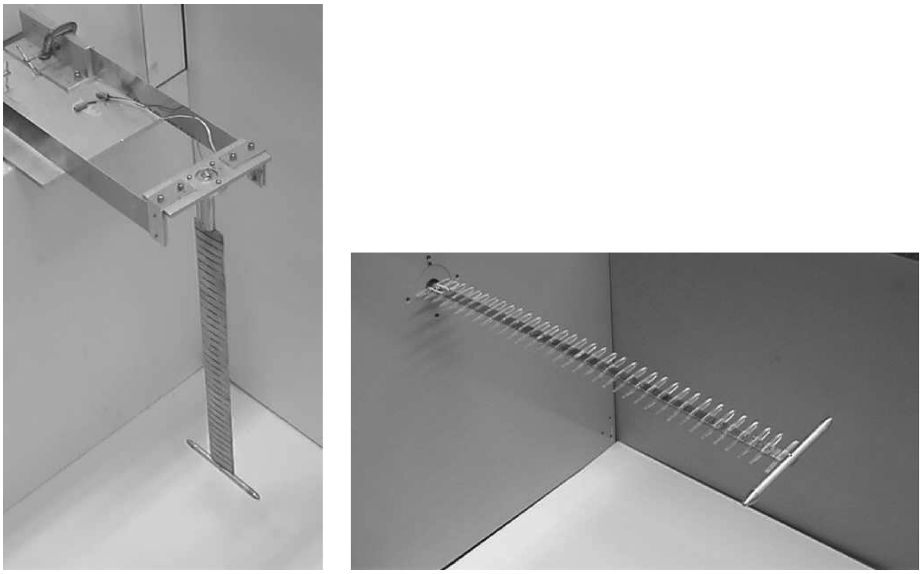

a) Experimental wing model b) Experimental wing model construction

Fig. 1 Photographs of the experimental wing model showing the flexible suspension and the wing model construction.

Table 1 Experimental wing model data

Wing properties	
Span (L)	0.4572 m
Chord (c)	0.0508 m
Mass per unit length	0.2384 kg/m
Mom. Inertia (50% chord)	0.2056×10^{-4} kg m
Spanwise elastic axis	50% chord
Center of gravity	49% chord
Flap bending rigidity (EI_1)	0.7466 Nm^2
Chordwise bending rigidity (EI_2)	0.2057×10^2 Nm^2
Torsional rigidity (GJ)	1.178 Nm^2
Flap structural modal damping (ξ_w)	0.02
Chordwise structural modal damping (ξ_v)	0.025
Torsional structural modal damping (ξ_ϕ)	0.031
Slender body properties	
Radius (R)	0.4762×10^{-2} m
Chord length (c_{SB})	0.1414 m
Total mass (M)	0.038 kg
Moment of inertia (I_{x0})	0.7956×10^{-4} kg m^2
Moment of inertia (I_y)	0.3456×10^{-6} kg m^2
Moment of inertia (I_{z0})	0.7956×10^{-4} kg m^2
Bi-beam support properties	
Material	Aluminum
Beam thickness	0.05 cm
Beam width	4.445 cm
Socket mass, M_r	0.2027 kg

tip twist response when it cooperates with the above micro-accelerometer at the tip.

The output signals from these transducers are directly recorded on a computer with data-acquisition and analysis software, Lab-VIEW 7.0.

The gust was created by placing a rotating slotted cylinder (RSC) behind a fixed airfoil upstream of the wing model. For details of the gust generator configuration and control, see [13].

All gust response tests were performed in the Duke University low speed wind tunnel. The wind tunnel is a closed circuit tunnel with a test section of $0.7 \times 0.53\ \mathrm{m}^2$ and a length of 1.52 m. The maximum air speed attainable is 89.3 m/ sec.

The basic parameters of the experimental wing model were obtained from standard static and vibration tests and are listed in the Table 1.

III. State-Space Theoretical Model

Figure 2 shows a schematic representation of the flexibly suspended HALE wing model. As shown in Fig. 2 the flexibly suspended HALE wing model includes two components. Component A is a HALE wing with a tip mass and component B is a flexible suspension system. The connection between components A and B uses an attached point, p. The dynamic analyses for the two components are described next.

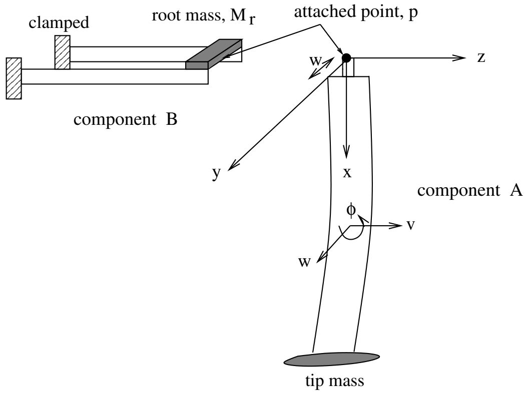

Fig. 2 Schematic representation of flexibly suspended HALE wing model.

A. Component A

According to the Hodges–Dowell equations [11], the equations of motion may be obtained, see Eqs. (1–3) of [7]. In these equations the gravitational effect is considered. The general mode shape functions are used these equations. They are expressed in series form as follows:

$$\bar{v} = \sum_{j=1}^{N_v} V_j(t)\nu_j(\bar{x}) \qquad \bar{w} = \sum_{j=1}^{N_w} W_j(t)\psi_j(\bar{x})$$

$$\phi = \sum_{j=1}^{N_\phi} \Phi_j(t)\varphi_j(\bar{x}) \tag{1}$$

where the overbar indicates nondimensionalization with respect to the wing span L, and ν_j, ψ_j, φ_j are the jth normal modes of the associated linear structural model. Note that ν_j and φ_j satisfy the clamped-free boundary conditions and ψ_j satisfy following boundary conditions:

$$\bar{x} = 0\text{:}\ \frac{\mathrm{d}\psi}{\mathrm{d}\bar{x}} = 0 \quad \text{and} \quad \frac{\mathrm{d}^3\psi}{\mathrm{d}\bar{x}^3} = 0$$

For $\bar{x} = 1$ it satisfies the free boundary conditions.

B. Component B

The dynamics of flexible root suspension system (bi-beam system) are considered in the present aeroelastic model. Using the Rayleigh–Ritz approach, the deflection of the suspension system is expressed in modal series form as follows:

$$\bar{s} = \sum_{k=1}^{M} S_k(t)\eta_k(\bar{y}) \tag{2}$$

where the overbar indicates nondimensionalization with respect to the bi-beam span, l, and η_k is the natural mode function and satisfies following boundary conditions:

$$\bar{y} = 0\text{:}\ \frac{\mathrm{d}\eta}{\mathrm{d}\bar{y}} = 0 \quad \text{and} \quad \frac{\mathrm{d}^3\eta}{\mathrm{d}\bar{y}^3} = 0$$

For $\bar{y} = -1$ the suspension bi-beam satisfies the clamped boundary conditions.

For the bi-beam with a tip mass M_r, the structural modal equation is expressed as a matrix equation as follows:

$$[M_b]\{\ddot{S}\} + [K_b]\{S\} = \{0\} \tag{3}$$

where the mass matrix $[M_b]$ consists of the generalized mass m_{sk} and the tip mass M_r with tip mode function. The stiffness matrix $[K_b]$ is a diagonal and depends on the generalized mass and natural frequency (ω_{sk}) of the bi-beam (without tip mass). Solving the above matrix equation, an eigensolution of the flexibly suspended system is determined. For the present system parameters (see Table 1) and bi-beam span, $l = 0.297$ m (the softest bi-beam stiffness) the first three natural frequencies are $\omega_{r1} = 1.708$ Hz, $\omega_{r2} = 27.79$ Hz and $\omega_{r3} = 76.48$. The associated eigenmodes are shown Fig. 3.

It is interesting to note that at the attached point ($\bar{y} = 0$) with the HALE wing, the first mode displacement is a maximum. This means the dynamic effect of the flexibly suspended system on HALE wing is significant. For the second and third modes, the mode displacements are small. Thus, for the present aeroelastic model and the gust frequency (lower than 40 Hz), only the first mode is considered in the calculations for simplicity. However, this simplifying assumption leads to a small error as described later in Sec. V. For the first mode, an equivalent spring stiffness, k_r, associated the flexibly suspended system is considered. This is

$$k_r = \omega_{s1}^2 m_{s1}$$

Because of $M_r \gg m_{sk}$, $k_r \approx M_r\omega_{r1}^2$. We use experiment to measure the first natural frequency, ω_{r1}, of the bi-beam support and to

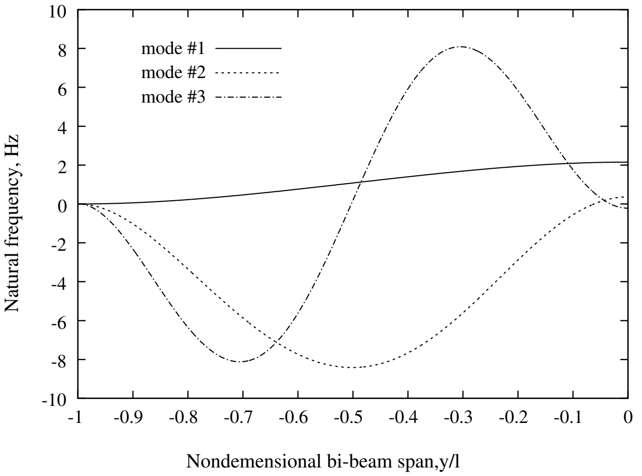

Fig. 3 First three eigenmodes for the flexibly suspended system at $l = 0.297$ m; $\omega_{r1} = 1.708$ Hz (1), $\omega_{r2} = 27.79$ Hz (2) and $\omega_{r3} = 76.48$ Hz (3).

determine the root equivalent spring stiffness. For five different bi-beam spans, l, the k_r are shown in Table 2.

The flexible suspension system now simplifies to a single degree of freedom oscillator with a displacement, s.

The constraint condition at the attached point, p, between the wing and the flexibly suspended system may be expressed as

$$w(0) - s = L\sum_{j=1}^{N} W_j(t)\psi_j(\bar{0}) - s = 0$$

The kinetic energy of the oscillator is

$$T^r = \frac{1}{2}M_r\dot{s}^2 = \frac{1}{2}M_r\dot{w}^2(0) = \frac{L^2}{2}M_r\left(\sum_{j=1}^{N}\dot{W}_j(t)\psi_j(\bar{0})\right)^2$$

and the potential energy is

$$V^r = \frac{1}{2}k_r s^2 = \frac{1}{2}k_r w^2(0) = \frac{L^2}{2}k_r\left(\sum_{j=1}^{N}W_j(t)\psi_j(\bar{0})\right)^2$$

C. Structural Modal Equation

Combining components A, B and the constraint condition and using Hamilton's principle and variational statement for δv, δu, δw, the final modal equation including structural and aerodynamic equation is expressed as follows:

$$\begin{aligned} m_{vi}\ddot{V}_i &+ \sum_{j=1}^{N_v}A_{vij}\ddot{V}_j + 2\omega_{vi}m_{vi}\xi_{vi}\dot{V}_i + m_{vi}\omega_{vi}^2V_i + \sum_{j=1}^{N_v}D_{vij}V_j \\ &+ \sum_{k=1}^{N_\phi}\sum_{j=1}^{N_w}K_{vijk}\Phi_kW_j = \int_0^1 \nu_i\frac{\mathrm{d}F_v}{\mathrm{d}x}\,\mathrm{d}\bar{x} + \nu_i(1)\Delta F_v \\ &i = 1, N_v \end{aligned} \tag{4}$$

Table 2 Equivalent spring stiffness k_r

Clamped position, l, cm	ω_{r1}, Hz	k_r N/m
29.7	1.6874	22.7625
24.7	2.2374	40.019
19.6	3.1124	77.4417
14.923	5.1349	209.968
9.700	7.814	487.925

$$\begin{aligned} m_{wi}\ddot{W}_i &+ \sum_{j=1}^{N_w}A_{wij}\ddot{W}_j + \sum_{j=1}^{N_\phi}S_{ij}\ddot{\Phi}_j + 2\omega_{wi}m_{wi}\xi_{wi}\dot{W}_i + m_{wi}\omega_{wi}^2W_i \\ &+ \sum_{j=1}^{N_w}D_{wij}W_j + \sum_{k=1}^{N_\phi}\sum_{j=1}^{N_v}K_{wijk}\Phi_kV_j = \int_0^1 \psi_i\frac{\mathrm{d}F_w}{\mathrm{d}x}\,\mathrm{d}\bar{x} \\ &+ \psi_i(1)\Delta F_w, \qquad i = 1, N_w \end{aligned} \tag{5}$$

$$\begin{aligned} I_{mi}\ddot{\Phi}_i &+ \sum_{j=1}^{N_\phi}A_{\phi ij}\ddot{\Phi}_j + \sum_{j=1}^{N_w}S_{ij}\ddot{W}_j + 2\omega_{\phi i}I_{mi}\xi_{\phi i}\dot{\Phi}_i + I_{mi}\omega_{\phi i}^2\Phi_i \\ &+ \sum_{k=1}^{N_w}\sum_{j=1}^{N_v}K_{\phi ijk}W_kV_j = \int_0^1 \varphi_i\frac{\mathrm{d}M_x}{\mathrm{d}x}\,\mathrm{d}\bar{x} + \varphi_i(1)\Delta M(x) \\ &i = 1, N_\phi \end{aligned} \tag{6}$$

where $\frac{\mathrm{d}F_w}{\mathrm{d}x}$, $\frac{\mathrm{d}F_v}{\mathrm{d}x}$ and $\frac{\mathrm{d}M_x}{\mathrm{d}x}$ are the aerodynamics contributed from the wing surface and ΔF_w, ΔF_v and ΔM_x are aerodynamic generalized forces from the slender body at the wing tip.

For the wing the ONERA aerodynamic stall model and wing strip theory assumption are used and for the slender body a linear slender body aerodynamic theory is used. For their detailed analysis, see [6,7].

The other coefficients are the following:

$$K_{vijk} = (EI_2 - EI_1)\int_0^1 \nu_i[\varphi_j\psi_k]''\,\mathrm{d}\bar{x}$$

$$K_{wijk} = (EI_2 - EI_1)\int_0^1 \psi_i[\varphi_j\nu_k]''\,\mathrm{d}\bar{x}, \qquad S_{ij} = \int_0^1 me\psi_i\varphi_j\,\mathrm{d}\bar{x}$$

$$K_{\phi ijk} = (EI_2 - EI_1)\int_0^1 \varphi_i[\nu_j''\psi_k'']\,\mathrm{d}\bar{x}, \qquad A_{\phi ij} = I_{x0}\varphi_i(1)\varphi_j(1)$$

$$A_{vij} = M\nu_i(1)\nu_j(1) + I_{y0}\nu_i'(1)\nu_j'(1)$$

$$A_{wij} = M\psi_i(1)\psi_j(1) + I_{z0}\psi_i'(1)\psi_j'(1) + M_r\psi_i(0)\psi_j(0)$$

$$D_{vij} = \int_0^1\left[\int_0^{\bar{x}} \nu_i'\nu_j'\,\mathrm{d}\bar{x}\right]\mathrm{d}\bar{x} + \int_0^1 \nu_i'\nu_j'\,\mathrm{d}\bar{x}$$

$$D_{wij} = \int_0^1\left[\int_0^{\bar{x}} \psi_i'\psi_j'\,\mathrm{d}\bar{x}\right]\mathrm{d}\bar{x} + \int_0^1 \psi_i'\psi_j'\,\mathrm{d}\bar{x} + k_r\psi_i(0)\psi_j(0)$$

D. Dynamic Perturbation Equations

Let $\{q\}$ be a state vector which is defined as

$$\{q\} = \{\dot{V}_j, V_j, \dot{W}_j, W_j, \dot{\Phi}, \Phi_j, C_{ll}, C_{ml}, C_{dl}\}$$

where the total structural mode number is $j = 1, 2, \ldots N_s$, and the aerodynamic section number along the span of the wing is $l = 1, 2, \ldots N_a$. C_{ll}, C_{ml}, C_{dl} are aerodynamic coefficients for the lth aerodynamic section obtained from ONERA aerodynamic equations.

One obtains a set of state-space matrix equations from Eqs. (4–6)

$$[\mathcal{A}]\{\dot{q}\} + [\mathcal{B}]\{q\} = \{F_0\}(\theta_0 + \alpha_G(t)) + \{F_N\} \tag{7}$$

Note the coefficient matrices, $[\mathcal{A}]$, $[\mathcal{B}]$ are dependent on the flow and structural parameters. The force vector F_0 is the linear static and gust loads obtained from the effects of steady and gust angle of attack and the force vector F_N is the nonlinear forces obtained from the structural nonlinearity and stall aerodynamics, respectively.

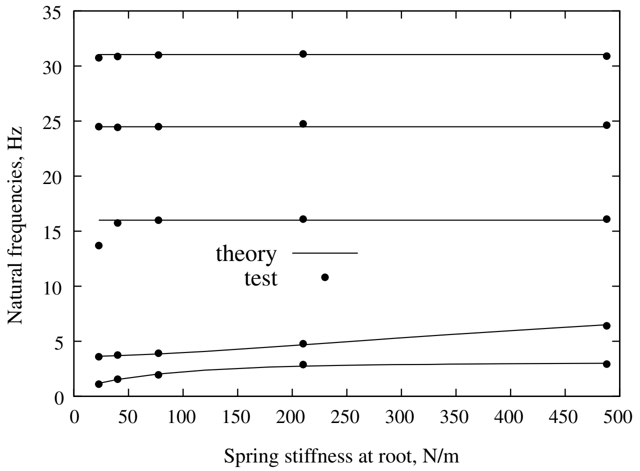

Fig. 4 Natural frequency vs spring stiffness at the root.

Equation (7) is a set of nonlinear equations of motion. For $F_N \neq 0$, $\alpha_{G0} = 0$ and $\theta_0 \neq 0$, a large static preflutter deformation may exist and then a dynamic perturbation approach is used to determine the small perturbation structural natural frequency and flutter boundary of this nonlinear system about a nonlinear and nontrivial static equilibrium condition. That is, one assumes

$$q = \bar{q} + \hat{q} \tag{8}$$

where the overbar refers to the static equilibrium value of the variable, and corresponding quantities with a symbol of ˆ are small (linear) dynamic perturbations about the static equilibrium state.

Substituting Eq. (8) into Eq. (7), a set of static equilibrium equations and dynamic perturbation equations is obtained. The static equilibrium equations comprise a set of nonlinear algebraic equations for the unknown state vector $\{\bar{q}\}$. In the present case, a direct time marching method is used to calculate the equilibrium solution.

The dynamic perturbation equations about a static equilibrium state are

$$[\bar{\mathcal{A}}]\{\dot{\hat{q}}\} + [\bar{\mathcal{B}}]\{\hat{q}\} = \{0\} \tag{9}$$

Note the coefficient matrices, $[\bar{\mathcal{A}}]$, $[\bar{\mathcal{B}}]$ are dependent on the flow velocity and the static equilibrium state, e.g., U, $\bar{q}$ etc.

IV. Preliminary Results

The calculations are based on the following choices for mode number and aerodynamic section number: The first four flap wing

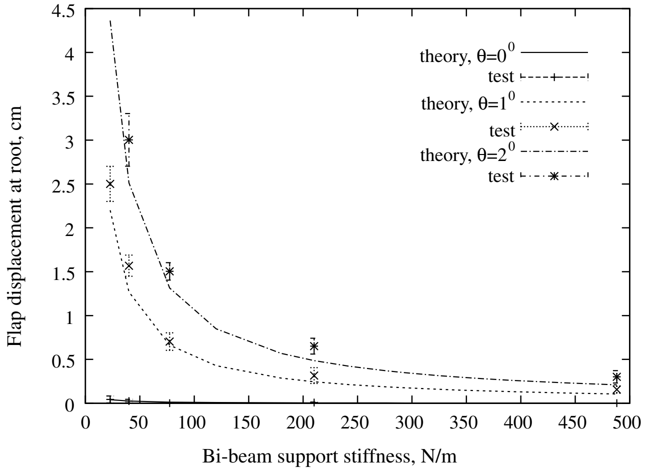

Fig. 5 Static displacement at root vs bi-beam support stiffness for $\theta_0 = 0, 1, 2°$.

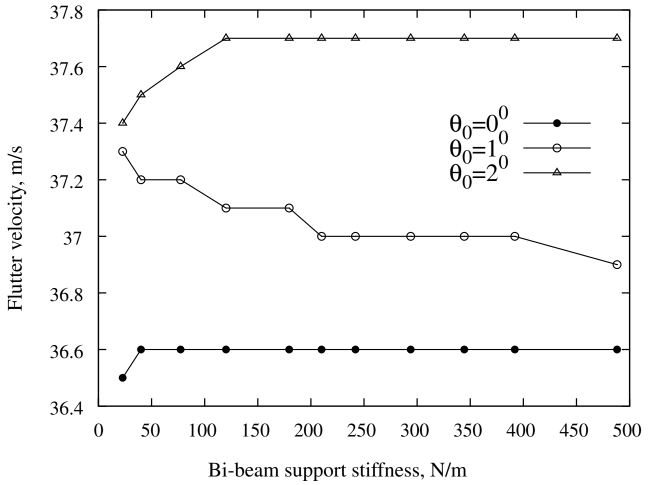

a) Flutter velocity

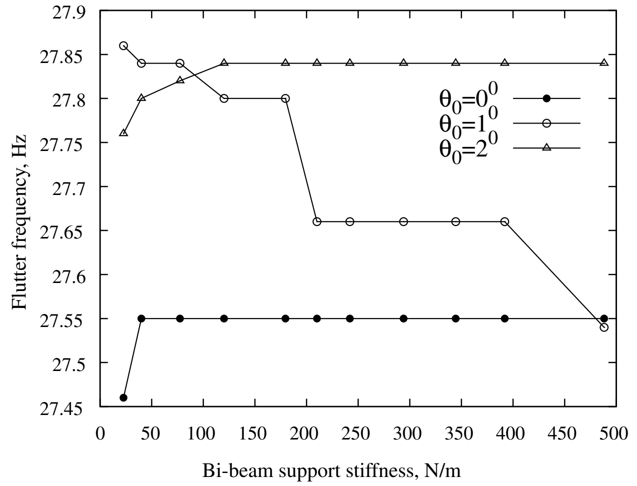

b) Flutter frequency

Fig. 6 Perturbation flutter solution of the nonlinear aeroelastic system for $\theta_0 = 0$, 1, 2° vs bi-beam support stiffness: a) flutter velocity and b) flutter frequency.

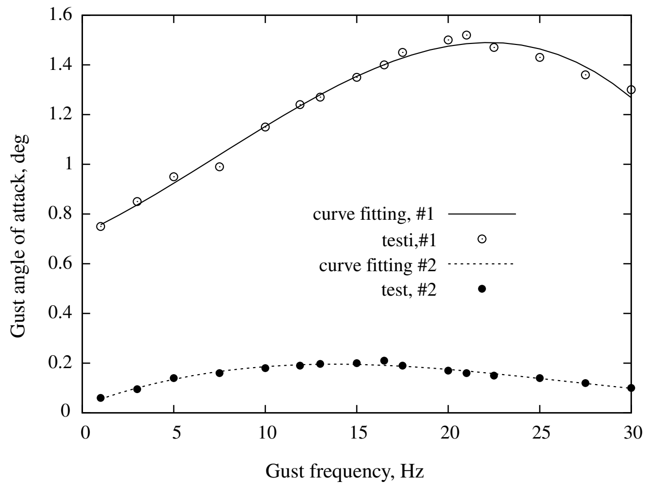

Fig. 7 Gust angle of attack vs gust frequency for $U = 18.5$ m/s. Experimental data points are indicated by the circles. Solid lines are curve fits. Numbers 1 and 2 indicate the first and second harmonic components of the gust.

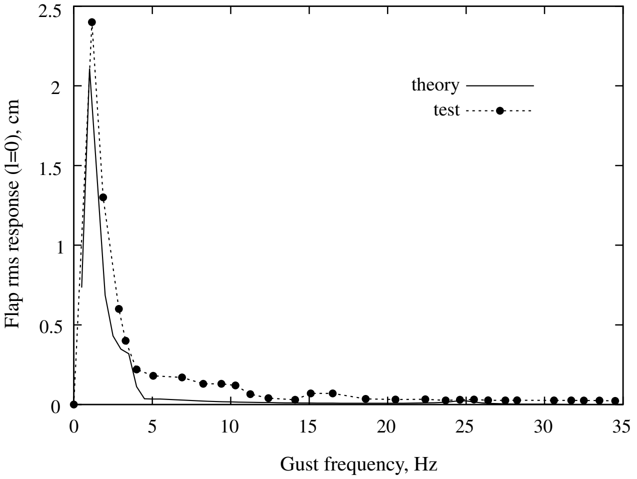

Fig. 8 Root displacement response to a harmonic gust excitation for bi-beam support stiffness, $k_r = 22.7\ \mathrm{N/m}$.

modes, first lag and first torsional modes are taken account. The wing is divided into ten [Eq. (10)] aerodynamic spanwise sections.

A. Effect of Bi-Beam Spring Stiffness on Natural Frequency

The computations of the natural frequency of the nonlinear aeroelastic model are based on the dynamic perturbation equation of Eq. (9) when the aerodynamic forces are set to be zero.

As shown in Table 2 the bi-beam span length, l, varies from 0.097 to 0.297 m and the equivalent bi-beam stiffness, k_r varies from 487.92 to 22.76 N/m. Figure 4 shows the first five natural frequencies of the flexibly suspended HALE wing model vs the root support stiffness. The effect of the stiffness on the natural frequency is significant only for first two flap natural frequencies for the range of spring stiffness shown. In the higher flap natural frequency range (above the second mode), they are almost independent of the bi-beam support stiffness, such as 24.7 Hz, which is dominated by second wing flap mode. Also the bi-beam support stiffness does not significantly affect the first lag natural frequency (15.7 Hz) and the first torsional frequency (30.5 Hz) of the wing mode.

The measurement data are also plotted in this figure. The agreement between the theory and experiment is good. In the lower flexible stiffness range, there is a larger error for the lag natural frequency. This may be because the lag boundary conditions do not exactly satisfy $\mathrm{d}v(0)/\mathrm{d}x = 0$ and $v(0) = 0$.

B. Effect of Bi-Beam Support Stiffness on Static Displacement at Root

Typical theoretical and experimental results of the static displacement at root vs the root stiffness are shown in Fig. 5 for several initial pitch angles of attack, $\theta_0 = 0$, 1, and 2°. The lines indicate the theoretical results and the bars indicate the measured data. The experimental data have some scatter due to the turbulent aerodynamic flow, although the flow noise is small. A very high measurement sensitivity is obtained from the displacement transducer, R30. A bar is used in the figure to indicate the magnitude of the experimental response uncertainty. As shown in Fig. 5, the flap root

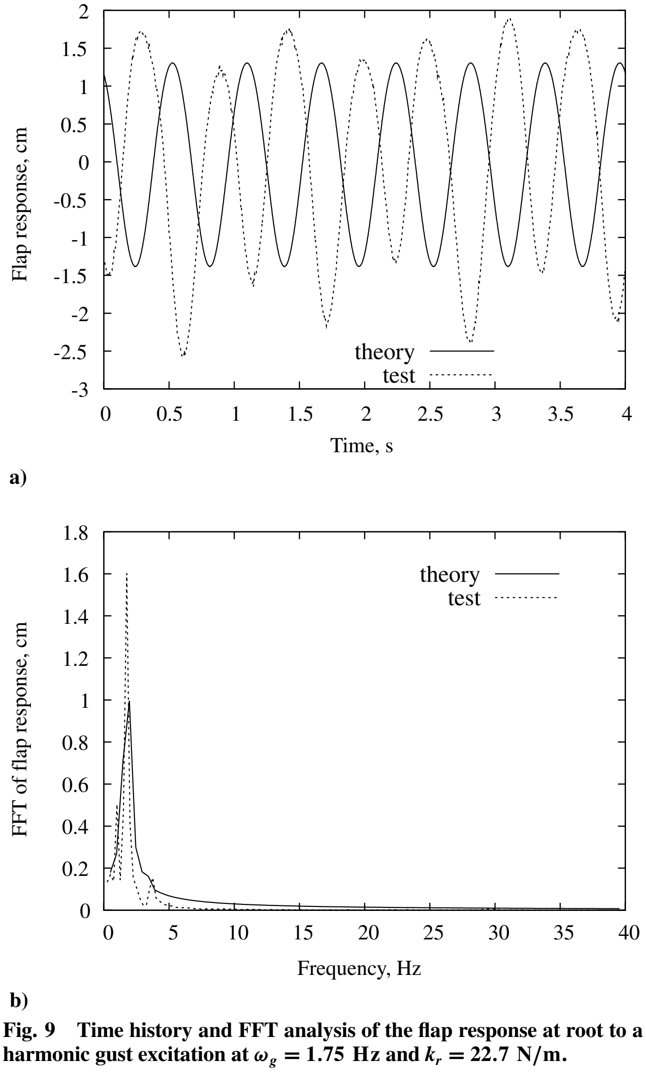

Fig. 9 Time history and FFT analysis of the flap response at root to a harmonic gust excitation at $\omega_g = 1.75$ Hz and $k_r = 22.7\ \mathrm{N/m}$.

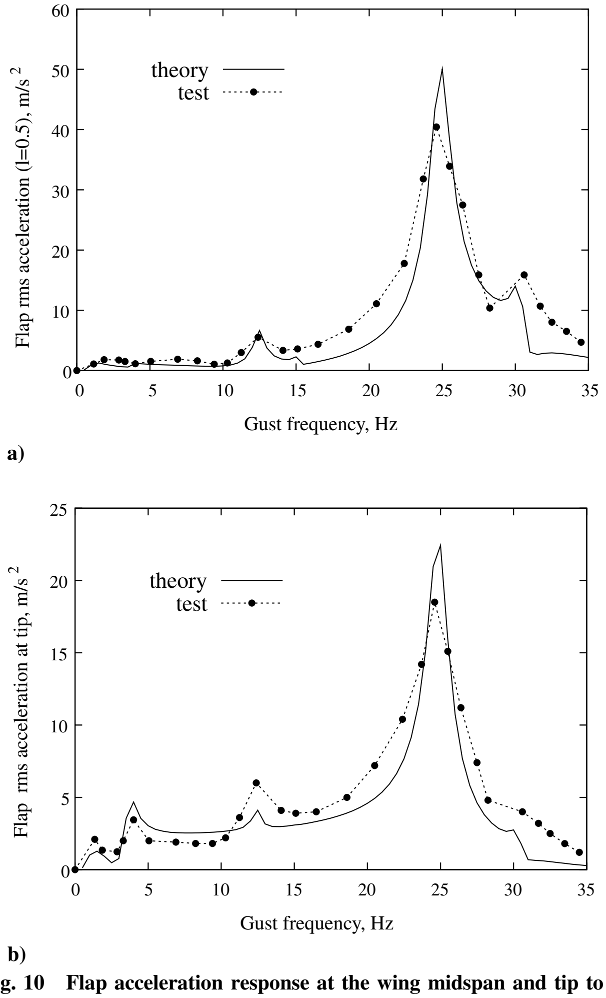

Fig. 10 Flap acceleration response at the wing midspan and tip to a harmonic gust excitation for bi-beam support stiffness, $k_r = 22.7\ \mathrm{N/m}$.

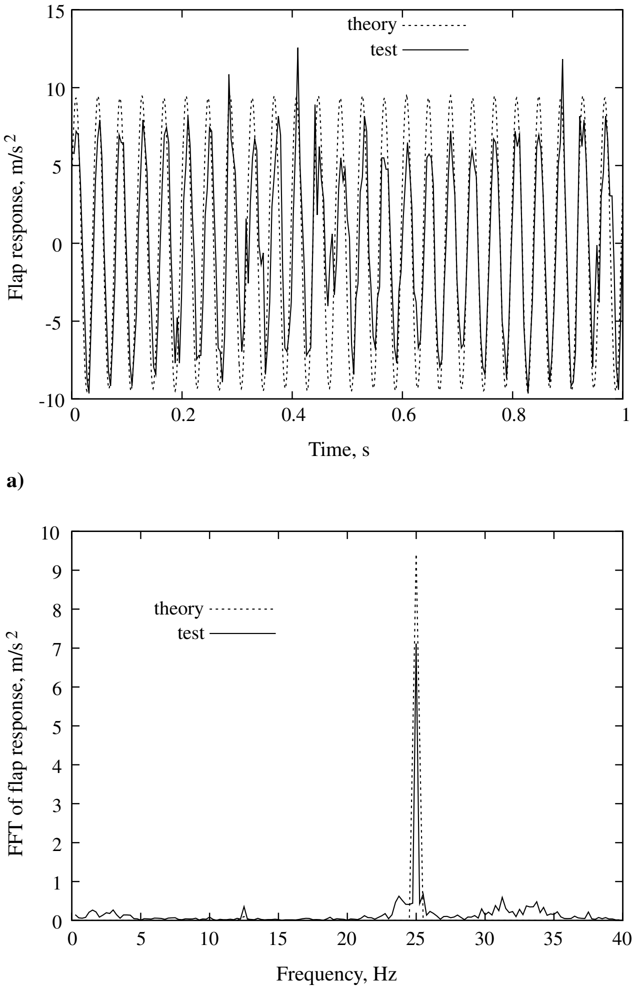

a)

b)

Fig. 11 Time history and FFT analysis of the flap response at root to a harmonic gust excitation at $\omega_g = 12.5$ Hz and $k_r = 22.7$ N/m.

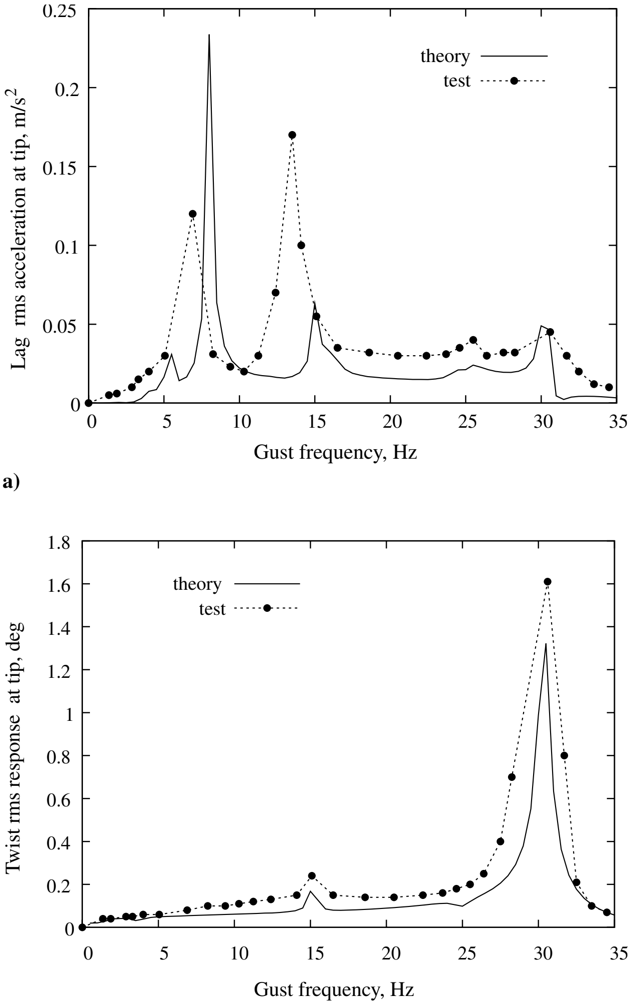

a)

b)

Fig. 13 Lag acceleration and twist response at the wing tip to a harmonic gust excitation for bi-beam support stiffness, $k_r = 22.7$ N/m.

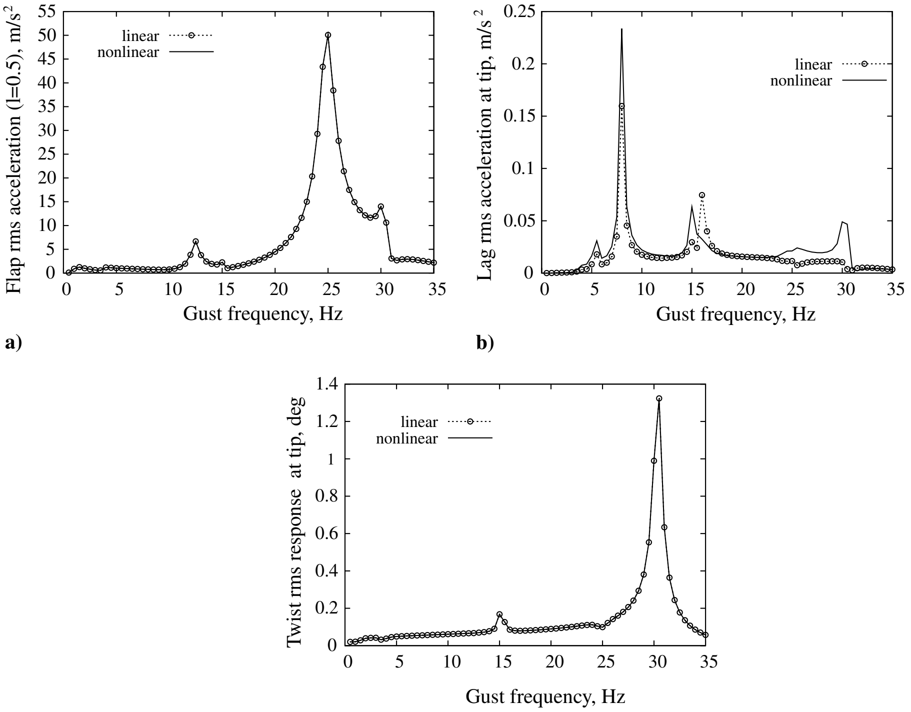

a)

b)

c)

Fig. 12 The effect of structural nonlinearity of flap, lag and twist responses for bi-beam support stiffness, $k_r = 22.7$ N/m.

displacement decreases with increasing bi-beam support stiffness. For $\theta_0 = 0°$ there is a very small displacement at the root in the lower stiffness range for the theory. This is due to a very small twist deflection created by the effect of structural nonlinearity. When the root pitch angle increases, the displacement increases significantly especially in the lower stiffness range. For $k_r = 22.7\ \mathrm{N/m}$ and $\theta_0 = 2°$, the measured static displacement is beyond the structural constraint range. The theoretical prediction and measured data in Fig. 5 are acquired before the onset of flutter and the flow velocity is $18.5\ \mathrm{m/s}$. In general, the agreement between theory and experiment is good, that is, within 10% or less.

C. Effect of Bi-Beam Spring Stiffness on Flutter

Using the nonlinear equations and a small perturbation flutter solution, the effect of bi-beam support stiffness at the root on flutter is considered. Several initial pitch angles are also considered.

Figure 6 shows the flutter velocity and frequency vs the bi-beam support stiffness for $\theta_0 = 0$, 1, and 2°.

As shown in Fig. 6 the effect of the root support stiffness on flutter is small because the flutter occurs based on the coupling between the third flap mode about 24.7 Hz and first torsional mode about 30.5 Hz. The effect of the suspended rigid body like mode on the third flap mode is very small as shown in Fig. 4. However note that the effect of the suspension system is to lower the flutter velocity, however, modestly, for some range of suspension stiffness and root angle of attack.

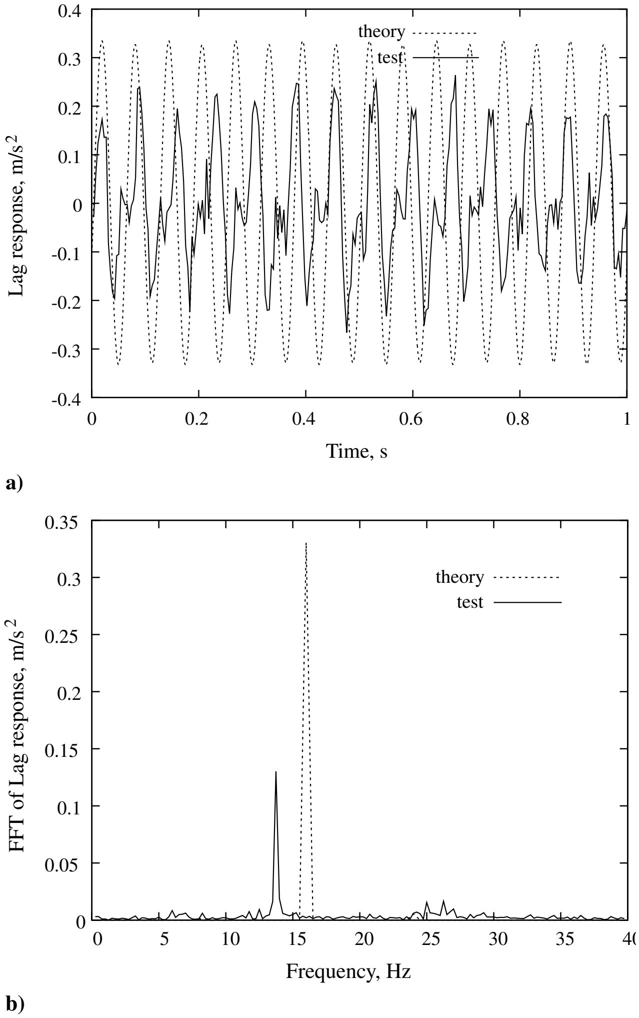

a)

b)

Fig. 14 Time history and FFT analysis of the lag response at wing tip to a harmonic gust excitation at $\omega_g = 8$ Hz for theory and $\omega_g = 6.8$ Hz for experiment.

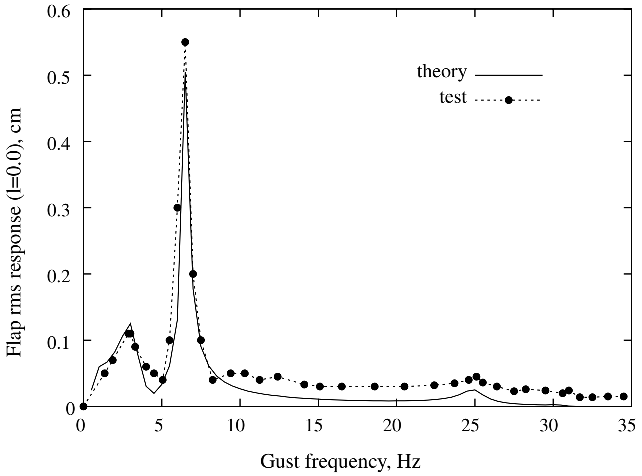

Fig. 15 Root displacement response to a harmonic gust excitation for bi-beam support stiffness, $k_r = 487.9\ \mathrm{N/m}$.

V. Results for Gust Response

A. Response to a Harmonic Gust Excitation

Equations (4–6) are used to calculate time marching response and the rms values shown in the following figures obtained from the steady state oscillation. The time step Δt is $1/2048$. Usually, the steady state is reached after about 10 s. The duration of the transient

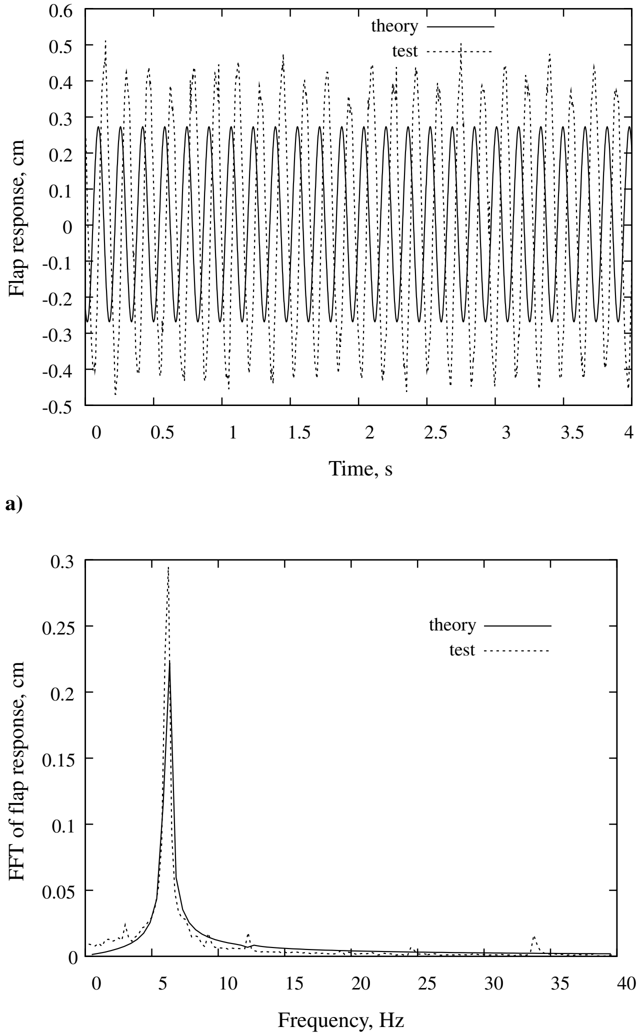

a)

b)

Fig. 16 Time history and FFT analysis of the flap response at root to a harmonic gust excitation at $\omega_g = 6.18$ Hz and $k_r = 487.9\ \mathrm{N/m}$.

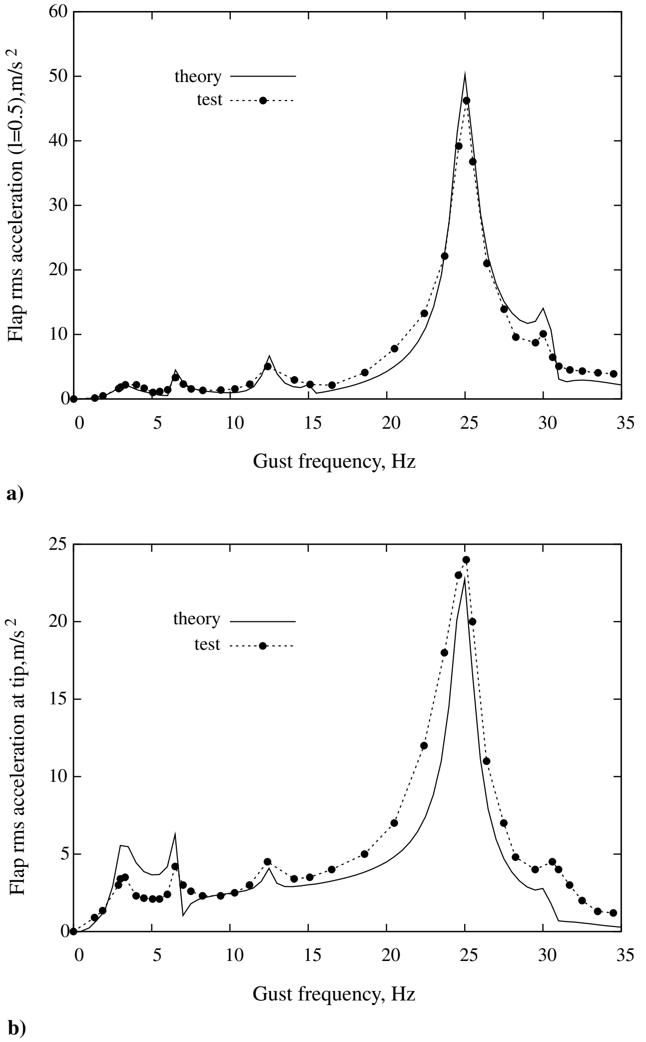

Fig. 17 Flap acceleration response at the wing midspan and tip to a harmonic gust excitation for bi-beam support stiffness, $k_r = 487.9$ N/m.

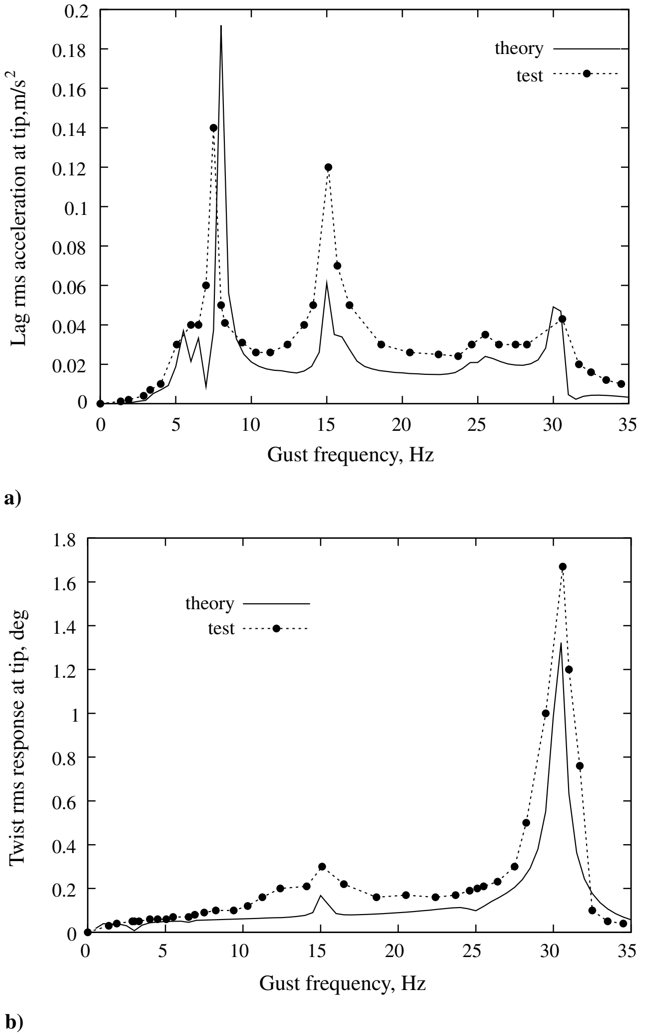

Fig. 18 Lag acceleration and twist response at the wing tip to a harmonic gust excitation for bi-beam support stiffness, $k_r = 487.9$ N/m.

response is largely determined by aerodynamic damping rather than structural damping for this model.

Two typical bi-beam support stiffnesses, $k_r = 22.76$ (lower) and 487.97 (higher) N/m, are used in the theoretical and experimental studies. These correspond to the suspended rigid body oscillation frequencies of 1.06 Hz and 6.5 Hz. The initial pitch angles of attack is set to $\theta_0 = 0°$. The flow velocity is 18.5 m/s.

The experimental sampling rate is 256 points/s, $\Delta t = 1/256$, and the total sampling length is 1024 points. For each gust frequency excitation, the data are acquired when the response achieves a steady state. The response is given by a rms value in the total sampling length both for the theoretical and experimental data.

Figure 7 shows the measured gust angle of attack (α_G) vs gust excitation frequency (Hz) for a flow velocity of $U = 18.5$ m/s. In this figure, a symbol, ○, indicates the measured first harmonic component and the symbol, ●, indicates the second harmonic component. The solid line is a least-square curve fitting of the experimental data. A formula based upon the measured experimental gust angle of attack is constructed as

$$\alpha_G(t) = \bar{\alpha}_{G1} \sin \omega t + \bar{\alpha}_{G2} \sin(2\omega t + \Delta\phi) \tag{10}$$

where $\Delta\phi$ is a possible phase difference between first and second gust frequencies. However, it is difficult to determine $\Delta\phi$ due to the flow field created by the present RSC gust generator. Thus, we assume $\Delta\phi = 0$ as an approximation.

Figure 8 shows the flap gust response at the root. This response particularly shows the rigid body mode. The resonant frequency is close to the first flap natural frequency as shown in Fig. 4. The typical time history and corresponding FFT analysis for $\omega_g = 1.75$ Hz are shown in Figs. 9a and 9b. From Fig. 9b of the FFT plot, a small peak is found at $\omega = 3.73$ Hz for the test data. This frequency corresponds to the second flap natural frequency. In general, the correlation between the theory and experiment is reasonably good for the frequency response curve.

Figures 10a and 10b show the flap acceleration response at the midspan (a) and tip (b) positions. As shown in both Figs. 10a and 10b, the main resonant frequency is at 25 Hz. At this frequency the agreement between the theory and experiment is not good, because this frequency is close to the second natural frequency of the bi-beam support system. The bi-beam vibration mode is clearly seen in the experimental video. Although the displacement amplitude of the attached point p is small, it still affects the wing flap response amplitude.

It is interesting to note that there is a small response at the gust excitation frequency, $\omega_g = 12.5$ Hz. The gust response is largest at a frequency of 25 Hz rather than the first harmonic excitation frequency, 12.5 Hz, as shown in Fig. 11 of the flap time history and FFT analysis at $\omega_g = 12.5$ Hz. Two reasons can be used to explain this phenomenon:

1) This is due to the gust second harmonic excitation. As shown in Fig. 7, at $\omega_g = 12.5$ Hz, $\alpha_{g1} = 1.26°$ and $\alpha_{g2} = 0.2°$.

2) This is due to structural nonlinearity. In Eqs. (4–6) the structural nonlinearity is the square term of the flap-lag-torsion coupled response. This term can create an excitation at double the gust first harmonic (12.5 Hz). Figures 12a–12c show the effect of the structural nonlinearity on the gust response. On these figures the structural

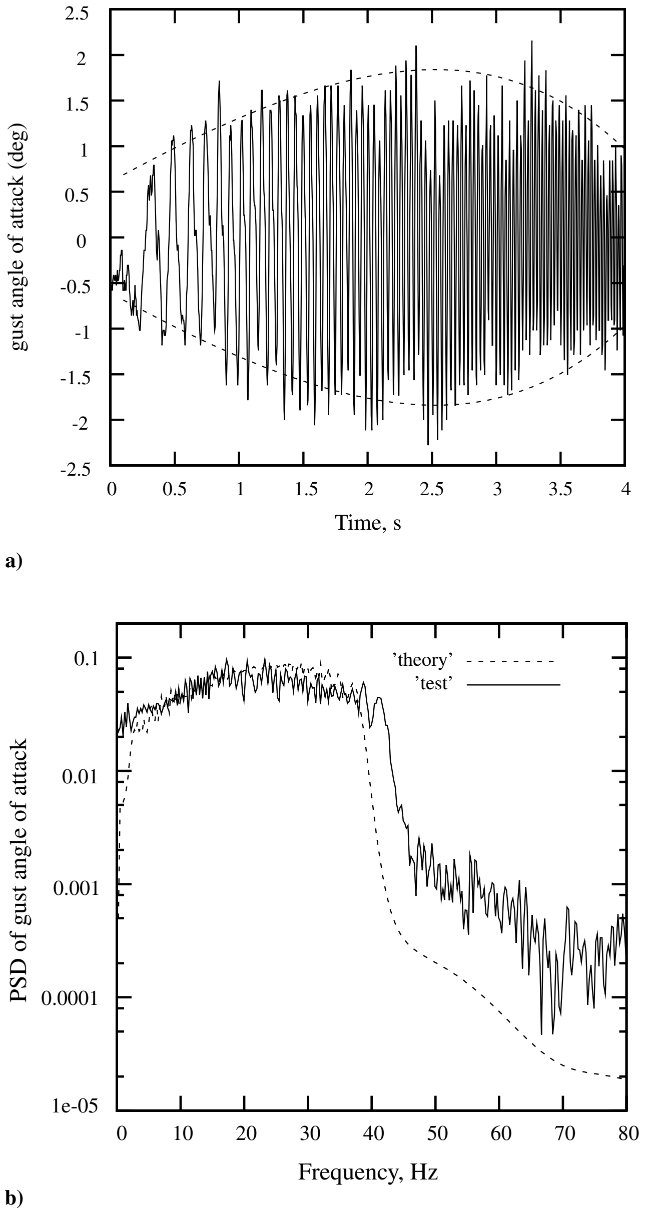

Fig. 19 Frequency sweep gust excitation for $U = 25\ \mathrm{m/s}$: a) time history, and b) PSD analysis.

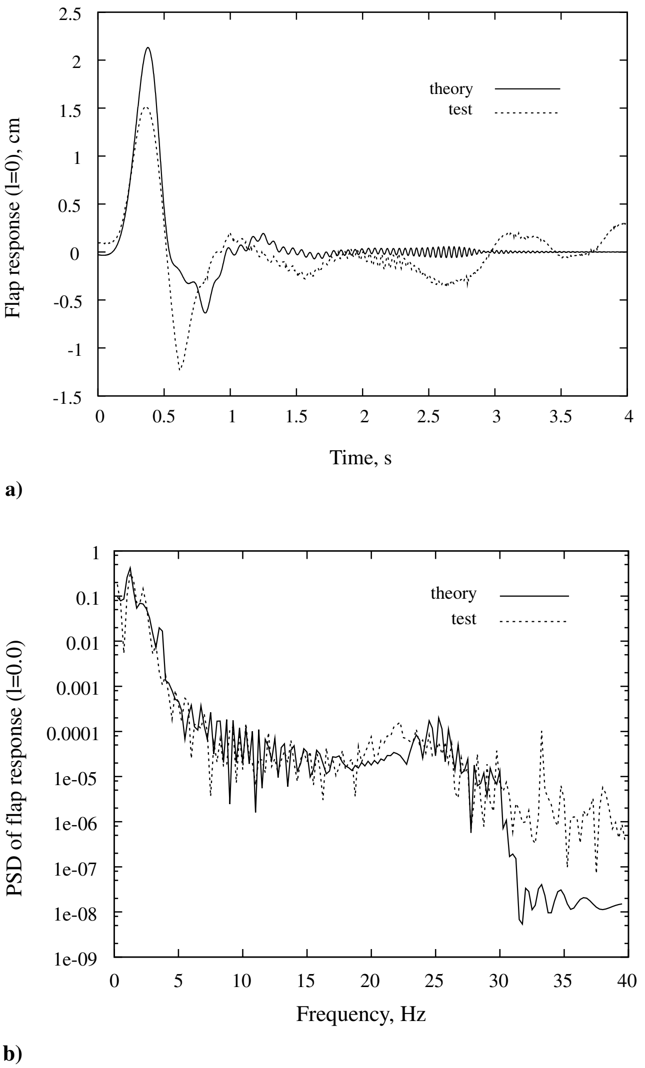

Fig. 20 Gust sweep response at the root for bi-beam support stiffness, $k_r = 22.7\ \mathrm{N/m}$: a) time history, and b) PSD analysis.

linear and nonlinear results are plotted for comparison. Figures 12a and 12c show the flap response at midspan and twist response at tip. The effect of the structural nonlinearity on the flap and twist responses is very small. This is because of a small lag response. As shown in the flap and torsional equations [Eqs. (5) and (6)], the nonlinear terms, $K_{wijk}\Phi_k V_j$ and $K_{\phi ijk} W_k V_j$ are dependent on the lag response V_j. When V_j is much smaller than W_j or Φ, this term becomes very small as shown in Figs. 12a and 12c. However, for the lag equation [Eq. (4)], the nonlinear terms, $K_{vijk}\Phi_k W_j$ are dependent of the flap and torsion responses W_j and Φ_k. When the W_j and Φ_k responses are larger, this nonlinear term becomes significant for the lag resonant response at 15.7 Hz as shown in Fig. 12b.

Comparing Figs. 10a and 10b, the rms amplitude at midspan is larger than the amplitude at the wing tip. The response mode at $\omega_g = 25$ Hz is near the flap third natural mode or wing second elastic mode.

Figures 13a and 13b show the lag acceleration response and twist response at the tip positions. As shown in Fig. 13a, the two main resonant frequencies are at 8 and 16 Hz from the theory and 6.8, 13.5 Hz from the test. Figures 14a and 14b show the theoretical and experimental time histories and corresponding FFT analysis for $\omega_g = 8$ Hz (theory) and 6.8 Hz (experiment). The principal gust response frequencies are 16 and 13.6 Hz rather than the gust excitation frequencies, 8 and 6.8 Hz, respectively. The agreement between the theory and experiment is not good. This is because of the boundary condition error in lag created by the flexible root support.

It is also interesting to note that there is a response peak near the gust frequency, $\omega_g = 8$ Hz for the theory and 6.8 Hz for the test. Similar to Fig. 10, this is due to the gust second harmonic excitation and the structural nonlinearity. The later effect seems stronger.

Figure 13b shows the twist gust responses at the wing tip. The main resonant response is at 30.5 Hz. At this frequency the agreement between the theory and experiment is reasonably good.

Similar to the lower bi-beam support stiffness, $k_r = 22.7\ \mathrm{N/m}$, the theoretical and experimental results for the higher bi-beam support stiffness, $k_r = 488.97\ \mathrm{N/m}$ are shown in the following figures.

Figure 15 shows the flap gust response at the root. There are two resonant frequencies to be found. The significant peak at $\omega_g = 6.5$ Hz shows the rigid body mode. The smaller peak is at $\omega_g = 3$ Hz and is close to the first flap natural frequency of the wing. The typical time history and corresponding FFT analysis for $\omega_g = 6.18$ Hz are shown in Figs. 16a and 16b. The correlation between the theory and experiment is reasonably good for the frequency response curve and time history.

Figures 17a and 17b show the flap acceleration response at the midspan (a) and tip (b) of the wing. Figures 18a and 18b show the lag acceleration response (a) and twist response at the tip of the wing.

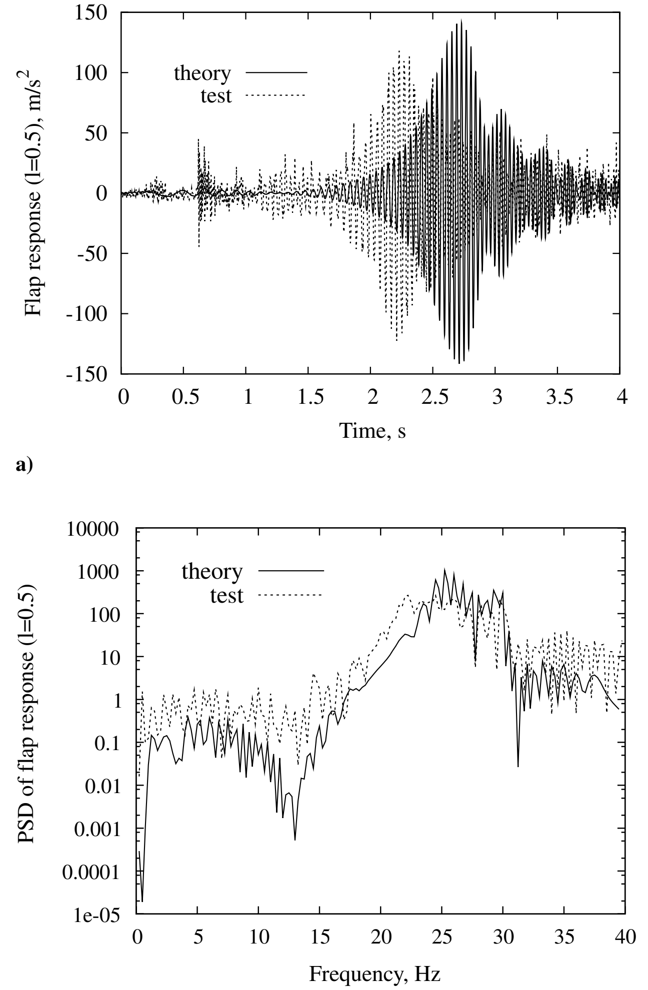

Fig. 21 Gust sweep response at the wing midspan for bi-beam support stiffness, $k_r = 22.7$ N/m: a) time history, and b) PSD analysis.

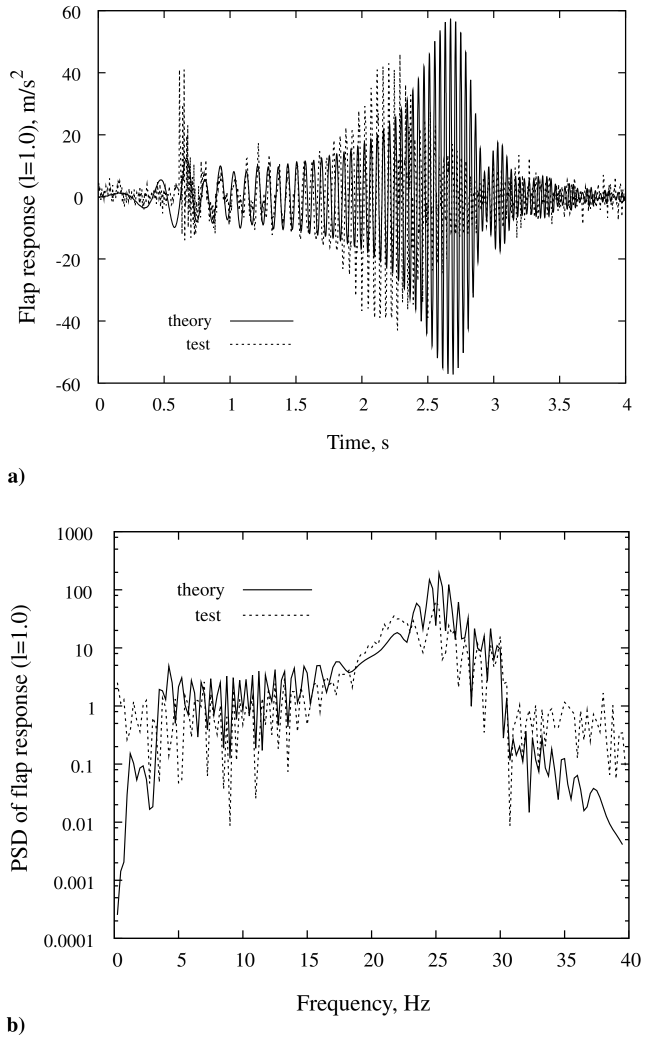

Fig. 22 Gust sweep response at the wing tip for bi-beam support stiffness, $k_r = 22.7$ N/m: a) time history, and b) PSD analysis.

Comparing the results for the two different bi-beam support stiffness, it is found that the following conclusions may be drawn.

1) The bi-beam support stiffness significantly affects the gust response in the lower gust frequency range for both the wing flap elastic motion and root body motion.

2) There is a small effect of the bi-beam support stiffness on the wing elastic response in the higher gust frequency range.

3) There is a very small effect of the bi-beam support stiffness on the lag and twist responses in the whole gust frequency range used.

4) The effect of the structural geometric nonlinearity on the flap and twist responses is smaller, but on the lag response is larger for the small gust load. The nonlinear structural forces create additional gust response (positive or negative) with the double gust frequency.

5) When the bi-beam support stiffness increases and the second natural frequency of the flexibly support system is beyond the gust frequency range an improved correlation between the theory and experiment is obtained for the wing flap responses and a lag response.

B. Response to a Frequency Sweep Gust Excitation

In this section we discuss the flap response due to a frequency sweep gust excitation. The flow velocity is set to be 25 m/s and the initial pitch angle is $\theta_0 = 0°$. The bi-beam support stiffness is set to $k_r = 22.7$ and $k_r = 487.9$ N/m.

Figure 19a shows a measured continuous linear frequency sweep gust angle of attack for $U = 25$ m/s. For the measured lateral gust, the minimum and maximum frequencies are 0 and 40 Hz, and the sweep duration T is 4 s. For convenient application in the gust response analysis, a formula based upon experimental gust angle of attack data is constructed

$$\alpha_G(t) = \bar{\alpha}_G(t)\sin\left(\omega_1 + \frac{\omega_2 - \omega_1}{2T}t\right)t \tag{11}$$

and where $\alpha_G(t)$ is given by

$$\bar{\alpha}_G(t) = \sum_{i=0}^{4} c_i t^i \tag{12}$$

and $c_0, \dots c_4$ are determined by a least-square curve fitting method from the experimental data.

An envelope of the numerical gust simulation is plotted in Fig. 19a as indicated by the broken line. Figure 19b shows a corresponding power spectra density (PSD) plot and comparison between the experimentally measured continuous linear frequency sweep gust (solid line) and the computational gust simulation (broken line) for $U = 25$ m/s.

The theoretical PSD results are obtained from an average over 10 sweep periods. The time step is $\Delta t = 1/2048$ and the sweep period is $T = 4$ s. The experimental time step is $1/256$ and the sweep period is $T = 4$ s. The total sampling length for one sweep period are 1024 points. The PSD results are obtained from an average over 10 sweep periods.

Figure 20a shows the theoretical and experimental time response histories to one sweep period gust excitation at the root for $K_r = 22.7$ N/m and Fig. 20b shows the corresponding PSD analysis. It is

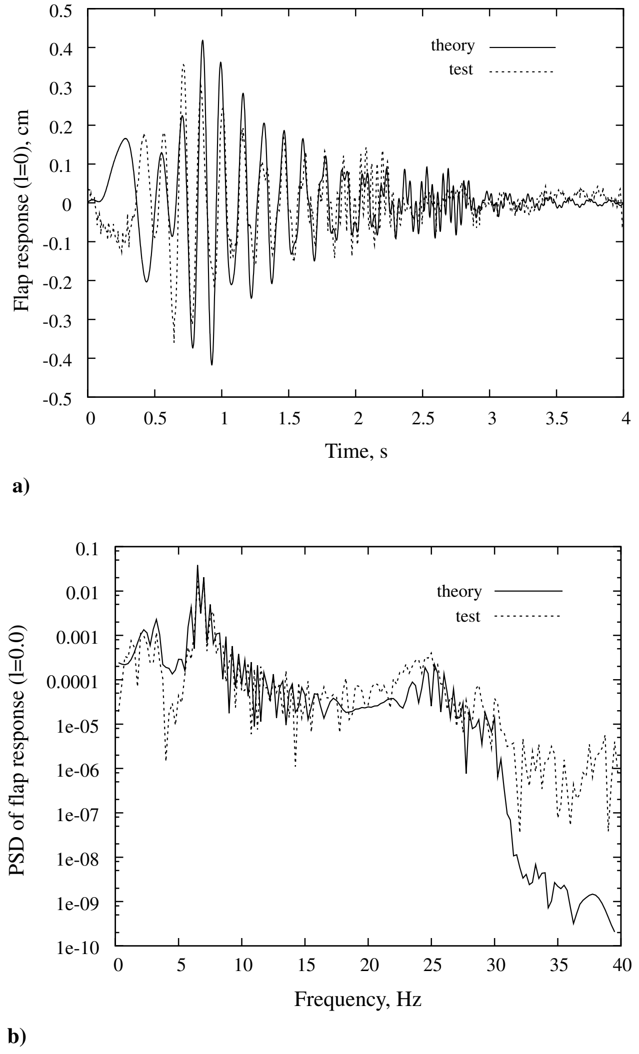

Fig. 23 Gust sweep response at the root for bi-beam support stiffness, k_r = 487.9 N/m: a) time history, and b) PSD analysis.

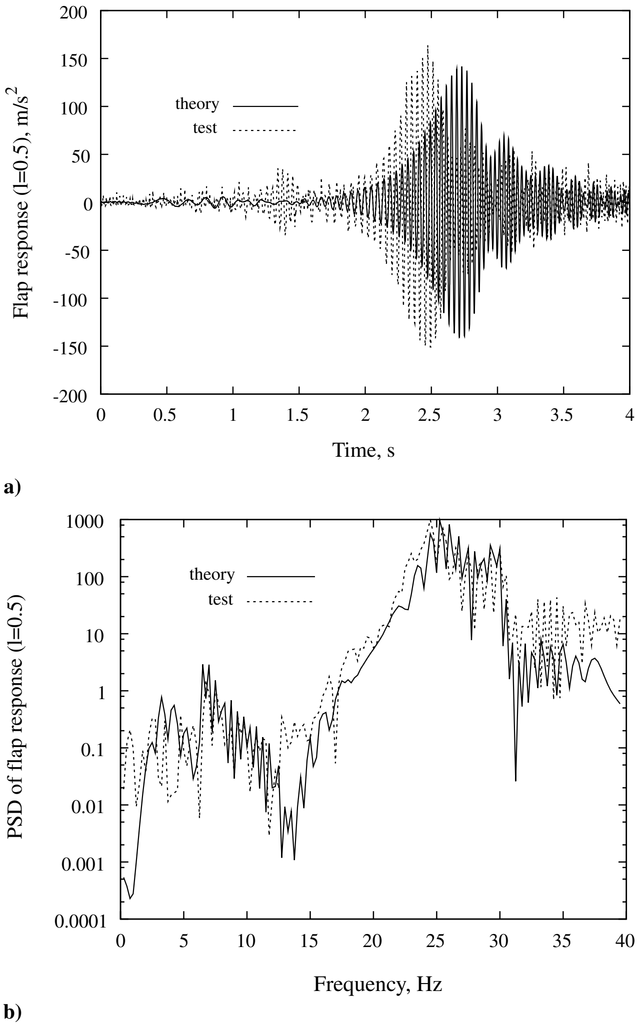

Fig. 24 Gust sweep response at the wing midspan for bi-beam support stiffness, k_r = 487.9 N/m: a) time history, and b) PSD analysis.

found that the spectral energy of the PSD concentrates at a gust frequency of 1.5 Hz and significantly excites the rigid body mode response. This confirms the results obtained from the sine-gust excitation as shown in Fig. 8.

Figure 21a shows the theoretical and experimental time histories to one sweep period gust excitation at the midspan for $k_r = 22.7$ N/m and Fig. 21b shows the corresponding PSD analysis. The spectral energy of the PSD has a maximum near a gust frequency of 25 Hz. The gust significantly excites the second wing elastic mode. Similar results are shown in Fig. 22 for the response at the wing tip. The agreement between the theory and experiment is reasonably good. These results are consistent with the results obtained from the sine-gust excitation as shown in Fig. 10.

Figures 23–25 shows the theoretical and experimental time histories to one sweep period gust excitation at the root, wing midspan and tip for $k_r = 487.9$ N/m and the corresponding PSD analysis.

Comparing the response to the gust sweep excitation for the two different bi-beam support stiffnesses, it is found that:

1) The response spectral energy distribution of PSD is significantly dependent on the bi-beam support stiffness in the lower gust frequency range for both the wing flap elastic motion and root body motion. This conclusion is consistent with the sine-gust results.

2) For the midspan and tip response, the spectral energy of the PSD concentrates at the flap natural frequency corresponding the wing second elastic mode, i.e., about 25 Hz, and it is almost independent of the bi-beam support stiffness.

To represent the gust response to the sweep frequency, in addition to using a PSD plot, another method is to use time rms response over one sweep period. In this case, five bi-beam support stiffnesses, $k_r = 22.7$, 40.3, 77.4, 210.5, and 487.9 N/m are considered in the experiment. Figures 26a–26c show the time flap rms response amplitude vs the bi-beam support stiffness from 22.7 N/m to 488.9 N/m at the root (a), the midspan (b) and the wing tip (c). As shown in Fig. 26a, the root rms amplitude decreases as k_r increases. As shown in Figs. 26b and 26c, the acceleration rms amplitude is almost a constant when k_r increases. The agreement between the theory and experiment is reasonably good. Recall that the root support flexibility in the lag and twist directions was not modeled in the computations.

C. Effect of Gust Distribution along the Span on Response

In this case it is assumed that the gust distribution along the span is a normal distribution

$$p(x) = \frac{1}{\sqrt{2\pi}\sigma} e^{-(x-m)^2/(2\sigma^2)}, \qquad 0 < x < 1$$

The gust loading is

$$\alpha_g(x,t) = p(x)\alpha_{g0}(t)$$

For comparison to the results of the basic gust loading, the distribution parameters, σ and m satisfy the following condition:

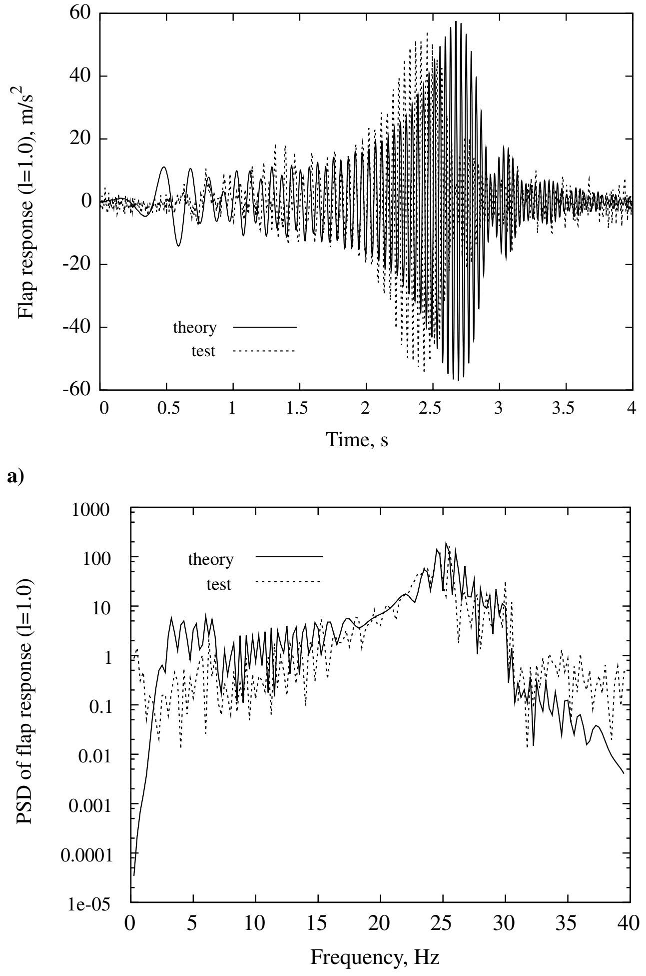

a)

b)

Fig. 25 Gust sweep response at the wing tip for bi-beam support stiffness, $k_r = 487.9$ N/m: a) time history, and b) PSD analysis.

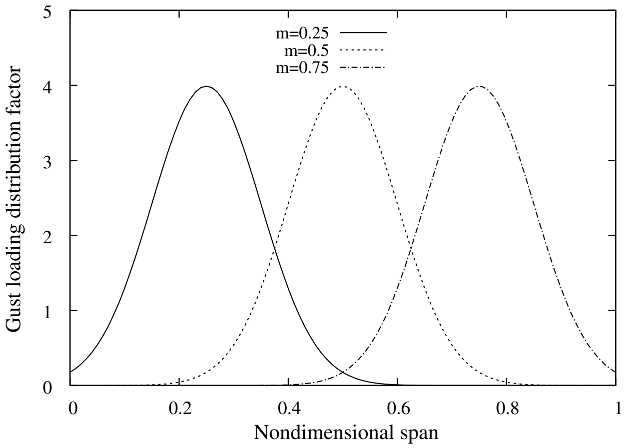

Fig. 27 Standard normal distribution along the wing span for different distribution parameters, $\sigma = 0.1$, $m = 0.25$, 0.5, and 0.75.

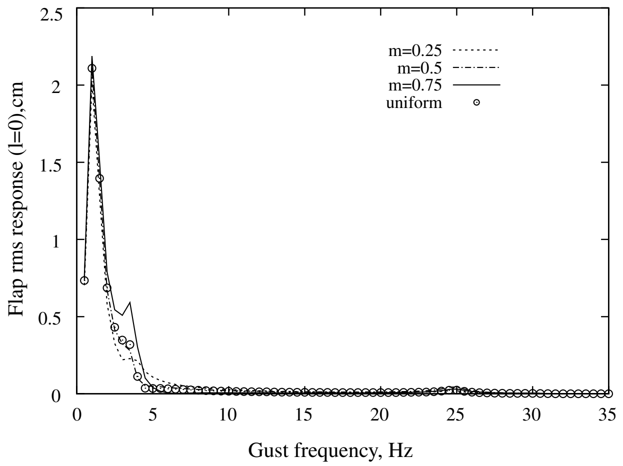

Fig. 28 Root displacement response to a harmonic gust excitation for bi-beam support stiffness, $k_r = 22.7$ N/m.

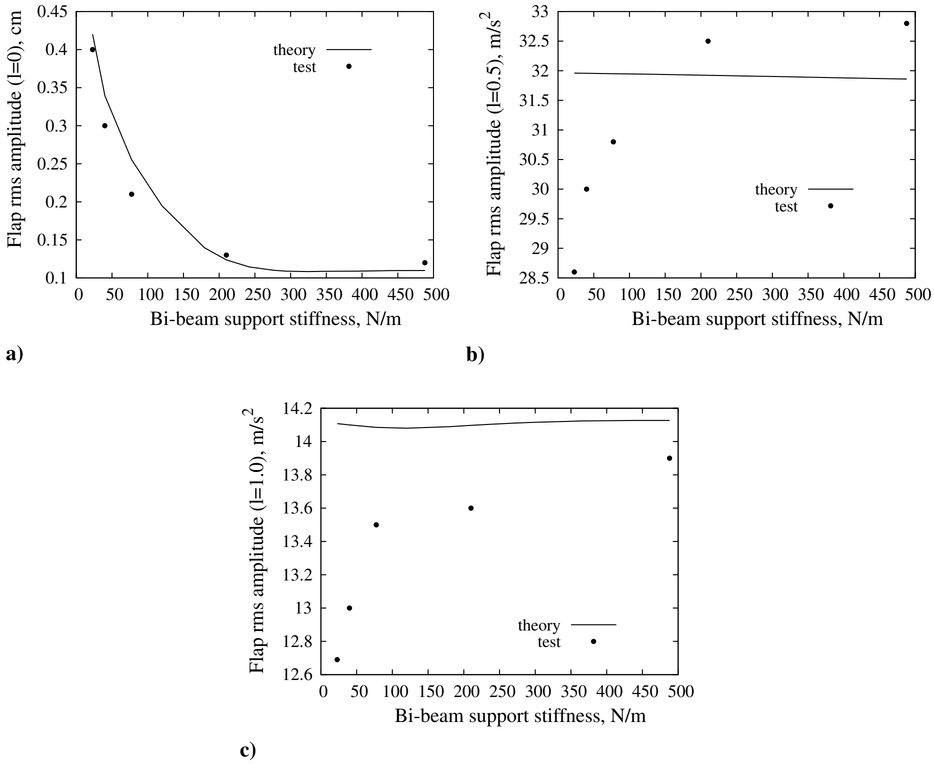

a)

b)

c)

Fig. 26 Flap rms gust response vs bi-beam support stiffness: a) at root, b) at wing midspan, and c) at wing tip.

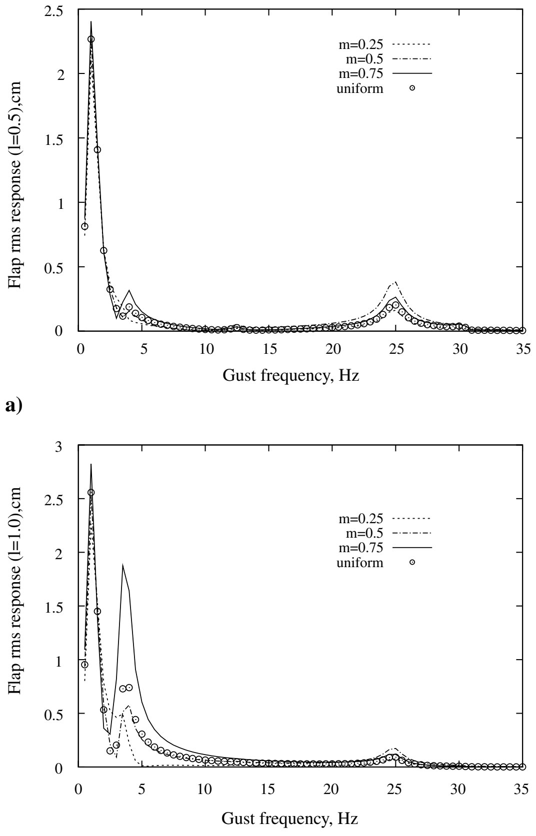

a)

b)

Fig. 29 Flap acceleration response at the wing midspan and tip to a harmonic gust excitation for bi-beam support stiffness, $k_r = 22.7$ N/m.

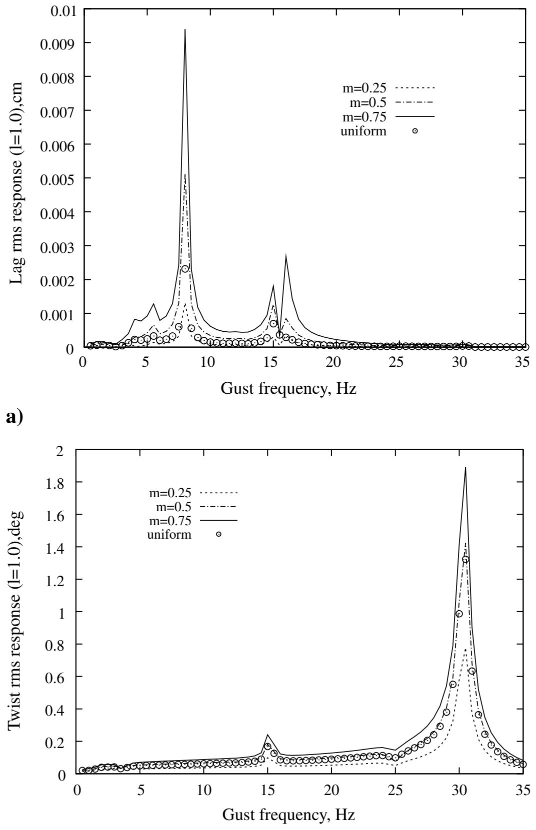

a)

b)

Fig. 30 Lag acceleration and twist response at the wing tip to a harmonic gust excitation for bi-beam support stiffness, $k_r = 22.7$ N/m.

$$\int_0^1 \alpha_g(x,t)\,\mathrm{d}x = \alpha_{g0}(t)$$

Thus, when $m = 0.25$ and $m = 0.75$, σ should be 0.09963 and for $m = 0.5$ σ is 0.10021.

The spanwise gust distributions, $p(x)$ for different paramaters, m and σ, are shown in Fig. 27.

The flap, chordwise and twist gust responses are shown in Figs. 28–30 for $m = 0.25, 0.5, 0.75$, and $\sigma = 0.09963$ and 0.10021. The results for uniform gust case are also plotted in these figures. A uniform gust has a gust distribution function of unity, $p(x) = 1$. As shown in these figures, the gust response depends significantly upon the gust center position along the span, i.e., the number m. As expected when the gust center moves toward the wing tip (larger m), the structural response is increased.

VI. Conclusions

1) The effect of a flexible mounting device at the wing root (to simulate a rigid body mode) has been shown to be modest for flutter based upon computations.

2) However the theoretical and experimental results show that the effect is significant for gust response both to a harmonic and a frequency sweep excitation in the lower gust frequency range. For the higher gust frequency range, the effect of the bi-beam support stiffness on the response is smaller.

3) Because a small gust load is used, the effect of geometric structural nonlinearity on the flap and twist responses is generally small.

4) The gust response is significantly dependent upon the gust center position along the span. When the gust center moves toward the wing tip, the structural response is increased.

References

[1] Van Shoor, M. C., and Von Flotow, A. H., "Aeroelastic Characteristics of a Highly Flexible Aircraft," *Journal of Aircraft*, Vol. 27, No. 10, 1990, pp. 901–908.
doi:10.2514/3.45955

[2] Patil, M. J., Hodges, D. H., and Cesnik, C. E. S., "Limit Cycle Oscillations in High-Aspect-Ratio Wings," *Journal of Fluids and Structures*, Vol. 15, No. 1, 2001, pp. 107–132.
doi:10.1006/jfls.2000.0329

[3] Patil, M. J., and Hodges, D. H., "On the Importance of Aerodynamic and Structural Geometric Nonlinearities in Aeroelastic Behavior of High-Aspect-Ratio Wings," *Journal of Fluids and Structures*, Vol. 19, No. 7, 2004, pp. 905–915.
doi:10.1016/j.jfluidstructs.2004.04.012

[4] Tang, D. M., and Dowell, E. H., "Effects of Geometric Structural Nonlinearity on Flutter and Limit Cycle Oscillations of High-Aspect Ratio Wings," *Journal of Fluids and Structures*, Vol. 19, No. 3, 2004, pp. 291–306.
doi:10.1016/j.jfluidstructs.2003.10.007

[5] Garcia, J. A., "Numerical Investigation of Nonlinear Aeroelastic Effects on Flexible High-Aspect-Ratio Wings," *Journal of Aircraft*, Vol. 42, No. 4, 2005, pp. 1025–1036.
doi:10.2514/1.6544

[6] Tang, D. M., and Dowell, E. H., "Experimental and Theoretical Study on Aeroelastic Response of High-Aspect Ratio Wings," *AIAA Journal*, Vol. 39, No. 8, 2001, pp. 1430–1441.

[7] Tang, D. M., and Dowell, E. H., "Experimental and Theoretical Study of Gust Response for A High-Aspect Ratio Wing," *AIAA Journal*, Vol. 40, No. 3, 2002, pp. 419–429.

[8] Tang, D. M., and Dowell, E. H., "Limit Cycle Hysteresis Response for A High-Aspect Ratio Wing Model," *Journal of Aircraft*, Vol. 39, No. 5, 2002, pp. 885–888.
doi:10.2514/2.3009

[9] Patil, M. J., Hodges, D. H., and Cesnik, Carlos E. S., "Nonlinear Aeroelasticity and Flight Dynamics of High-Altitude, Long-Endurance Aircraft," *Journal of Aircraft*, Vol. 38, No. 1, 2001, pp. 88–94.
doi:10.2514/2.2738

[10] Patil, M. J., and Taylor, D. J., "Gust Response of Highly Flexible Aircraft," *Proceedings of the 47th Structures, Structural Dynamics, and Materials Conference*, 2006-1638, AIAA Reston, VA, May 2006.

[11] Hodges, D. H., and Dowell, E. H., "Nonlinear Equations of Motion for the Elastic Bending and Torsion of Twisted Nonuniform Rotor Blades," NASA TN D-7818, 1974.

[12] Tran, C. T., and Petot, D., "Semi-Empirical Model for the Dynamic Stall of Airfoils in View to the Application to the Calculation of Responses of a Helicopter Blade in Forward Flight," *Vertica*, Vol. 5, No. 1, 1981, pp. 35–53.

[13] Tang, D. M., Paul, G. A. Cizmas., and Dowell, E. H., "Experiments and Analysis for A Gust Generator in A Wind Tunnel," *Journal of Aircraft*, Vol. 33, No. 1, Jan.–Feb. 1996, pp. 139–148. doi:10.2514/3.46914

E. Livne
Associate Editor